Quadratic dynamical decoupling with nonuniform error suppression

Gregory Quiroz and Daniel A. Lidar

Phys. Rev. A **84**, 042328 — Published 17 October 2011

DOI: 10.1103/PhysRevA.84.042328

Quadratic Dynamical Decoupling with Non-Uniform Error Suppression

Gregory Quiroz
Department of Physics and Center for Quantum Information Science & Technology, University of Southern California, Los Angeles, California 90089, USA

Daniel A. Lidar
Departments of Electrical Engineering, Chemistry, and Physics, and Center for Quantum Information Science & Technology, University of Southern California, Los Angeles, California 90089, USA

We analyze numerically the performance of the near-optimal quadratic dynamical decoupling (QDD) single-qubit decoherence errors suppression method [J. West *et al*., Phys. Rev. Lett. **104**, 130501 (2010)]. The QDD sequence is formed by nesting two optimal Uhrig dynamical decoupling sequences for two orthogonal axes, comprising N_1 and N_2 pulses, respectively. Varying these numbers, we study the decoherence suppression properties of QDD directly by isolating the errors associated with each system basis operator present in the system-bath interaction Hamiltonian. Each individual error scales with the lowest order of the Dyson series, therefore immediately yielding the order of decoherence suppression. We show that the error suppression properties of QDD are dependent upon the parities of N_1 and N_2, and near-optimal performance is achieved for general single-qubit interactions when $N_1 = N_2$.

PACS numbers: 03.67.Pp, 03.65.Yz, 82.56.Jn, 76.60.Lz

I. INTRODUCTION

In recent years, there have been promising advances towards the usage of quantum systems to perform quantum information processing (QIP) [1]. However, for these systems to be utilized efficiently, it is necessary to preserve and store information for a sufficient amount of time so that computations can be implemented. Unfortunately, quantum systems are generally hindered in their ability to perform such tasks effectively due to unwanted interactions between the system and its enviroment, which result in decoherence [2].

Dynamical Decoupling (DD) is a strategy that can be used to suppress decoherence and effectively remove unwanted system-environment interactions for a period of time such that quantum states can be preserved with a low probability of error [3]. As originally conceived, DD schemes are characterized by the application of short control pulses to the system such that the overall time evolution provided by the pulses selectively average out system-environment interactions, thereby suppressing decoherence [4–7]. One advantage of DD is that it is an open-loop control method, which does not require any measurements or feedback, unlike quantum error correction [8]. Nor does DD require any specific knowledge of the environment other than it being non-Markovian, unlike optimal control methods designed to suppress decoherence [9, 10].

Early DD schemes were designed to remove unwanted system-bath interactions to a given, low order in time-dependent perturbation theory [3]. Concatenated DD (CDD) was the first explicit scheme capable of removing such interactions to an arbitrary order [11]. CDD accomplishes this via a recursive construction in which each successive level removes another order in time-dependent perturbation theory. The advantages of CDD over standard periodic pulse sequences have been extensively studied analytically [12, 13] and numerically [12, 14–17], and confirmed in a number of recent experimental studies [18–22]. However, assuming that pulse intervals can be made arbitrarily short, the number of pulses required to achieve arbitrary order suppression grows exponentially with the order in CDD. When the finiteness of pulse intervals is accounted for there is an optimal level of concatenation and correspondingly a highest attainable perturbation theory order for removal of unwanted interactions [12, 13, 19].

In contrast to CDD, Uhrig DD (UDD) is characterized by the use of unequal pulse intervals, or free evolution periods [23]. By applying control pulses at

$$t_j = T \sin^2 \frac{j\pi}{2(N+1)}, \tag{1}$$

where $j = 1, 2, \ldots, N+1$, a UDD sequence of total duration T yields Nth order decoupling for single-axis system-bath coupling [24]. The number of pulses comprising a UDD sequence is N if N is even, or $N+1$ if N is odd. Generalizations of UDD for generic system-environment interactions include Concatenated UDD (CUDD) [25], Quadratic Dynamical Decoupling (QDD) [26] and Nested Uhrig Dynamical Decoupling (NUDD) [27] (see also [28]). CUDD removes the restriction of single-axis decoupling and suppresses general (three-axis) decoherence errors on a qubit, but still suffers from the exponential cost of CDD. On the other hand, QDD also suppresses general decoherence errors on a qubit, but does so without the exponential cost of CDD by nesting two UDD sequences for two orthogonal axes. In fact, QDD is a near-optimal scheme for single-qubit decoupling from an arbitrary bath, requiring only N^2 pulses for Nth order decoupling if N is even, or $(N+1)^2$ pulses if N is odd. The NUDD sequence is built on the same nesting idea, but removes the QDD restriction of single-qubit decoupling. NUDD applies to arbitrary multi-level systems coupled to arbitrary baths, as recently proved in Ref. [29].

In this work we focus on the decoherence errors suppres-

sion capabilities of QDD. This protocol requires two nested sequences each containing N_j pulses if N_j is even or $N_j + 1$ pulses if N_j is odd, $j = 1, 2$. We call N_1 and N_2 the inner and outer sequence order, respectively. While the original QDD paper [26] noted that sequences with $N_1 \neq N_2$ are possible and could be advantageous when a particular axis is dominant, only the case $N_1 = N_2$ was analyzed. Here we numerically study QDD for $N_1 \neq N_2$. We provide a complete numerical elucidation of the performance of QDD as a function of N_1 and N_2.

Our numerical analysis assumes that the system-bath interaction and internal bath Hamiltonian are bounded in operator norm. This assumption works well for various spin-bath models of relevance to solid-state quantum computing, such as electron spin qubits coupled to a nuclear spin bath as found, e.g., in quantum dots [30]. It does not work as well for oscillator-bath models, where the internal bath Hamiltonian has divergent operator norm, unless a high-frequency cutoff is introduced. See, e.g., Ref. [13] for a detailed discussion of this issue.

The structure of this paper is as follows. In Section II we provide a brief synopsis of our results. In Section III we summarize the QDD protocol. In Section IV we introduce the relevant error measures utilized in this paper and provide an analysis of the expected scaling of these measures with the inner and outer sequence orders. Section V is devoted to our numerical results. In it we discuss the scaling of the single-axis errors and their time-dependence, as well as the scaling of a distance measure for the entire QDD sequence. Section VI presents our conclusions.

II. SYNOPSIS OF RESULTS

We characterize QDD performance with respect to the order of error suppression given by the overall fidelity loss of the qubit (system) state. We show that the order of overall error suppression is dictated by the lowest of the inner or outer sequence orders, namely $D \sim (J\tau)^{\min\{N_1,N_2\}+1}$, where D is a measure of the overall error, J is the strength of the system-bath coupling, and τ is the smallest pulse interval.

To arrive at these results and gain more insight we first characterize QDD performance with respect to the order of error suppression given by the order of error suppression along each axis of the qubit Bloch sphere, referred to as the single-axis error. We isolate the single-axis errors by projecting the total evolution operator into the three directions defined by the Pauli basis. The error suppression properties are then distinguished with respect to the scaling of the error as a function of the minimum pulse interval for various inner and outer sequence orders. Since this scaling is dominated by the first non-zero term of the Dyson series, the order of error suppression for each single-axis error can be characterized with respect to inner and outer sequence order. Suppression of the x-axis error (or "X-type error") is determined by N_1, the y-axis error by the parity of N_1 and N_2, and the z-axis error by N_2 except in the case when N_1 is odd [see Eqs. (35)-(37)]. Our results will show that if N_1 is odd, there is a constraint on the suppression of the z-axis error depending on the value of N_1 with respect to N_2.

Parity effects were anticipated in Ref. [27], where the expected performance of QDD was proved for sequences with even N_1 (the proof was recently completed in Ref. [29]). We show that parity effects are absent in QDD only for the interaction that anti-commutes solely with the decoupling operator comprising the inner sequence. This interaction (σ^x) is suppressed with UDD efficiency, i.e., N_1th order error suppression for a pulse sequence comprising N_1 pulses. This result holds for the outer sequence as well (i.e., the σ^z interaction, except in the case of $N_2 \geq 2(N_1 + 1)$ with N_1 odd, where the inner sequence hinders the ability of the outer sequence to suppress decoherence to the expected order. We find that in general, UDD efficiency for general single-qubit errors is achieved when N_1 and N_2 are both even.

We introduce another perspective on the QDD sequence, by studying the time-dependence of the single-axis errors. We find that as the sequence progresses, these errors oscillate between values that are near to their final minimum, and much higher values.

III. QDD PROTOCOL

UDD suppresses single-qubit dephasing or longitudinal relaxation errors *separately*, for a general environment [31, 32]. The extension of UDD to QDD improves on this by handling general single-qubit decoherence, in particular both dephasing and relaxation simultaneously. Therefore, in our analysis of QDD the time-independent Hamiltonian

$$H = H_B + H_{SB}, \tag{2}$$

$$H_B = I \otimes B_I, \tag{3}$$

$$H_{SB} = \sigma^x \otimes B_x + \sigma^y \otimes B_y + \sigma^z \otimes B_z \tag{4}$$

is employed to describe general system-environment interactions for the single-qubit system. The system operators σ^μ are the standard Pauli matrices, while the bounded operators, B_μ, $\mu \in \{I, x, y, z\}$, characterize a generic environment. The operator B_I encompasses the pure bath dynamics, so that H_B is the "pure-bath" Hamiltonian, while H_{SB} is the system-bath interaction Hamiltonian.

In building a QDD sequence to compensate for the interactions present in the above Hamiltonian, it is useful to first choose a so-called Mutually Orthogonal Operator Set (MOOS) [27]. This set comprises mutually anti-commuting or commuting operators needed to perform DD in the general NUDD scheme. Each of these operators is required to anti-commute with some portion of the interaction Hamiltonian. The anti-commutation condition between an element of the MOOS and the interaction Hamiltonian is essential for decoherence suppression. One might expect a UDD sequence composed of an element of the MOOS to suppress the corresponding anti-commuting interaction with UDD efficiency. As we shall show, this is not the case, except for the inner sequence.

In the case of a single-qubit system, NUDD reduces to QDD and the MOOS requires only two operators. There is

some flexibility in choosing the MOOS for Eq. (2), but without loss of generality we pick $\Omega = \{X, Z\}$. The operators $X = \sigma^x \otimes I$ and $Z = \sigma^z \otimes I$ (we drop global phase factors everywhere) represent ideal zero-width π-rotations about their respective axes of the qubit subspace, and do not affect the bath. The QDD sequence is now readily constructed as [26]

$$U_{\Omega}^{(N_1,N_2)} = X^{N_2} Z^{(N_1)}(s_{N_2+1}\tau) \cdots X Z^{(N_1)}(s_1\tau), \quad (5)$$

where

$$Z^{(N_1)}(\tau) = Z^{N_1} U(s_{N_1+1}\tau) \cdots Z U(s_2\tau) Z U(s_1\tau). \quad (6)$$

Note that the order of nesting (Z into X or X into Z) is immaterial for our purposes. The free evolution dynamics between successive pulses, $U(t) = e^{-iHt}$, is governed by Eq. (2), and the free evolution time durations are given in terms of the normalized UDD intervals,

$$s_j = \frac{t_j - t_{j-1}}{t_1 - t_0}, \quad (7)$$

with t_j specified by Eq. (1), and $\tau = t_1 - t_0$. The high efficiency of UDD in suppressing decoherence, and therefore QDD, arises from the choice of the relative free evolution time durations $\{s_j\}$.

The total normalized time of an N-pulse UDD sequence is given by,

$$S^{(N)} \equiv \sum_{j=1}^{N+1} s_j = \frac{t_{N+1}}{t_1} = \csc^2\left(\frac{\pi}{2N+2}\right), \quad (8)$$

so that the total physical time is

$$T^{(N)} = S^{(N)}\tau. \quad (9)$$

Therefore the total normalized time of a QDD sequence with N_1 inner and N_2 outer pulses is given by,

$$\begin{aligned} S^{(N_1,N_2)} &\equiv \sum_{j=1}^{N_2+1} s_j S^{(N_1)} \\ &= \csc^2\left(\frac{\pi}{2N_1+2}\right) \csc^2\left(\frac{\pi}{2N_2+2}\right), \end{aligned} \quad (10)$$

so that the total physical time is $T^{(N_1,N_2)} = S^{(N_1,N_2)}\tau$.

IV. QDD PERFORMANCE MEASURES

A. QDD analysis

Our goal here is to understand the properties of QDD error suppression for general N_1 and N_2 and for a wide range of parameters. We do so by isolating the errors proportional to each system basis operator, σ^μ, $\mu = \{x, y, z\}$, i.e., the single-axis errors. In this manner the order of error suppression can be extracted directly and possible constraints on QDD effectiveness can be accurately identified. Each single-axis error is obtained from the evolution operator, $U_{\Omega}^{(N_2,N_1)}$, by projecting along the particular axis of interest and performing a partial trace over the system. The order of error suppression can then be quantified by the scaling of the single-axis error as a function of either the total evolution time or the minimum pulse interval. We choose the minimum pulse interval since experimentally this quantity is always lower-bounded, and plays an important role in the ultimate performance limits of UDD [32] and DD in general [33].

The resulting QDD evolution operator, $U_{\Omega}^{(N_2,N_1)}$, contains all the information regarding decoherence suppression for each single-axis error. Construction of the final evolution operator is accomplished by first considering the inner sequence evolution, $Z^{(N_1)}(\tau)$. Let Eq. (2) be partitioned such that $H = H_+ + H_-$, where

$$H_+ = \sigma^x \otimes B_x + \sigma^y \otimes B_y \quad (11)$$

and

$$H_- = I \otimes B_I + \sigma^z \otimes B_z. \quad (12)$$

Clearly, the element of the MOOS comprising $Z^{(N_1)}(\tau)$ anti-commutes with H_+ and commutes with H_-, i.e., $[H_\pm, Z]_\pm = 0$, where the plus and minus sign subscripts signify the anti-commutator and commutator, respectively.

The Z-type UDD sequence $Z^{(N_1)}(\tau)$ is effective against the anti-commuting Hamiltonian, H_+. $Z^{(N_1)}(\tau)$ is completely ineffective against unwanted interactions within H_-. Any additional errors associated with H_- must be addressed using another member of the MOOS. The inner sequence evolution can be expanded in terms of $H_\pm$ [24],

$$\begin{aligned} Z^{(N_1)}(\tau) \;=\; & e^{-i[(-1)^{N_1}H_+ + H_-]s_{N_1+1}\tau} \cdots \\ & \cdots e^{-i[-H_+ + H_-]s_2\tau} e^{-i[H_+ + H_-]s_1\tau}, \end{aligned} \quad (13)$$

where the anti-commuting and commuting properties of $H_\pm$, respectively, have been used. Transforming into the interaction picture with respect to H_-, we can write $Z^{(N_1)}(\tau) = U_-^{(N_1)}(\tau) U_z^{(N_1)}(\tau)$, such that $U_-^{(N_1)}(\tau) = e^{-iH_- S^{(N_1)}\tau}$ and

$$U_z^{(N_1)}(\tau) = \hat{\mathcal{T}} \exp\left(-i \int_0^{S^{(N_1)}\tau} f_z(t) H_+(t) dt\right). \quad (14)$$

The modulation function $f_z(t) = (-1)^{j-1}$ is defined for $t \in [\sum_{\ell=1}^{j-1} s_\ell\tau, \sum_{\ell=1}^{j} s_\ell\tau]$ and $\hat{\mathcal{T}}$ is the time-ordering operator. H_+ in the rotating frame with respect to H_- takes on the form of a power series expansion in t,

$$H_+(t) = U_-^{(N_1)\dagger}(t) H_+ U_-^{(N_1)}(t) = \sum_{k=0}^{\infty} H_+^{(k)} t^k. \quad (15)$$

The power series form of $H_+(t)$ is useful (though not essential [27]) for the proof of UDD and therefore the suppression of error associated with H_+ [31, 32, 34, 35]. All constants of the

expansion are condensed within $H_+^{(k)}$, along with the k-fold commutator

$$[{}_kH_-, H_+] = [H_-, [H_-, \cdots [H_-, H_+]\cdots]]. \tag{16}$$

Using time-dependent perturbation theory, $U_z^{(N_1)}(\tau)$ is expanded in the Dyson series

$$U_z^{(N_1)}(\tau) = \sum_{n=0}^{\infty} \sum_{\mathbf{k}_n} H_+^{(k_n)} \cdots H_+^{(k_1)} F_z^{(N_1,\mathbf{k}_n)}(\tau), \tag{17}$$

where $\mathbf{k}_n = \{k_1, ..., k_n\}$ with $k_i = 0, 1, ...$ for all i, and all of the time-dependence of the expansion has been placed in

$$F_z^{(N_1,\mathbf{k}_n)}(\tau) = (-i)^n \int_0^{S^{(N_1)}\tau} \int_0^{t_{n-1}} \cdots \int_0^{t_2} \prod_{j=1}^{n} dt_j \, f_z(t_j) t_j^{k_j} \tag{18}$$

The proof of UDD is completed by parametrizing t_j as $t_j = \tau \sin^2(\theta_j/2)$, Fourier expanding $f_z(t_j)$, and showing that $F_z^{(N_1,\mathbf{k}_n)}(\tau) = 0$ for all odd values of n when $n + \sum_{j=1}^{n} k_j \leq N_1$ [24]. All even orders of the expansion are proportional to unity or σ^z, and are therefore not associated with H_+. The expansion ultimately yields

$$Z^{(N_1)}(\tau) = e^{-iH'_-(\tau)S^{(N_1)}\tau + \mathcal{O}\left((\tau\|H'_+(\tau)\|)^{N_1+1}\right)}, \tag{19}$$

where $H'_+(\tau)$ is a generic single-qubit system-bath Hamiltonian and

$$H'_-(\tau) = B'_I(\tau) + \sigma^z \otimes B'_z(\tau) \tag{20}$$

is composed of environment operators dependent on the minimum pulse interval. Note that these environment operators are not the same operators defined in Eq. (2), but combinations of the original Hamiltonian operators resulting from the perturbation expansion.

Left with only dephasing errors, terms proportional to σ^z, the process is continued again by defining $\tilde{H}_+ = \sigma^z \otimes B'_z(\tau)$ and $\tilde{H}_- = B'_I(\tau)$ for the outer X-type UDD sequence of Eq. (5). $\tilde{H}_\pm$ is defined in this way such that $[\tilde{H}_\pm, X]_\pm = 0$, a similar condition to that required for the inner Z-type sequence. The resulting evolution of Eq. (5) can be summed up as

$$U_\Omega^{(N_1,N_2)} = B''_I(\tau) + \sum_{\mu\in\{x,y,z\}} \sigma^\mu \otimes B''_\mu(\tau). \tag{21}$$

Once again, the time-dependent environment operators, $B''_\mu(\tau)$, differ from the previously defined environment operators. Each $B''_\mu(\tau)$, $\mu \in \{x, y, z\}$, contains the uncompensated decoherence along each of the qubit axes. Bounds on the order of error suppression are derived analytically in Ref. [36].

B. Single-axis errors

One of our goals is to characterize the performance of QDD with respect to the remaining system-environment interaction operators, $B''_\nu(\tau)$. The error is quantified by what we refer to as the single-axis error E_μ:

$$E_\mu(\tau) = \|B''_\mu(\tau)\|_F, \tag{22}$$

where

$$B''_\mu(\tau) = \mathrm{Tr}_S\left(U_\Omega^{(N_1,N_2)}\sigma^\mu\right), \tag{23}$$

and where $\|A\|_F$ is the Frobenius norm of A, i.e.,

$$\|A\|_F = \mathrm{Tr}\sqrt{A^\dagger A}, \tag{24}$$

the sum of singular values of A. (The choice of norm is somewhat arbitrary; we could have used any other unitarily invariant norm [37].) Thus $E_\mu(\tau) \geq 0$, and we are interested in how the single-axis errors scale as a function of the minimum pulse interval.

C. Distance measure

The advantage of the single-axis error over other measures such as polarization or fidelity is that these typically scale with the overall minimum order of decoherence suppression and therefore do not provide detailed information about the structure of the unitary evolution operator itself. However, the single-axis errors of course do not tell the whole story of QDD performance. A useful overall fidelity-loss measure is the distance [38]

$$D(U, G) = \frac{1}{\sqrt{d_S d_B}} \min_\Phi \|U - G \otimes \Phi\|_F, \tag{25}$$

Here d_S and d_B denote the dimensions of the system and bath Hilbert spaces, respectively, U is the actual system-bath unitary evolution operator, G is the desired system-only unitary operator, and Φ is a bath operator. Grace *et al*. [38] give an explicit form for this distance measure, so that in our numerical simulations we do not need to compute the minimum over Φ. In our case $G = I$ is the desired system unitary operator since the goal of DD is to remove the system-environment interaction while effectively acting trivially on the system. The advantage of the distance measure $D(U, G)$ of Eq. (25) over the standard Uhlman fidelity or trace-norm distance [39] is that it is state-independent and can be correlated directly with the results obtained for the single-axis errors.

We shall show that $D(U, I)$ scales in the same manner as $\min_\mu E_\mu(\tau)$. It will also illuminate some interesting features of QDD based on the inner sequence order not captured by the single-axis errors.

D. Scaling

We parametrize the strength of the pure environment dynamics and system-environment interactions, respectively, as

$$\beta = \|H_B\|, \quad J = \|H_{SB}\|, \quad J_\alpha = \|B_\alpha\| \tag{26}$$

where $\|A\|$ is the standard sup-operator norm, namely the largest singular value (largest eigenvalue of $\sqrt{A^\dagger A}$):

$$\|A\| = \sup_{|\psi\rangle} \frac{\sqrt{\langle\psi|A^\dagger A|\psi\rangle}}{\sqrt{\langle\psi|\psi\rangle}}. \tag{27}$$

The effectiveness of DD tends to be greater in the regime where the environment is essentially static and the duration of the free evolution is much smaller than the environment correlation time: $J\tau \ll 1$ and $\beta \ll J$.

We model the environment as a four-qubit bath with operators

$$B_\mu = \sum_{i\neq j} \sum_{\alpha,\beta} c^\mu_{\alpha\beta} \left(\sigma_i^\alpha \otimes \sigma_j^\beta\right) \tag{28}$$

characterizing the dynamics of the bath and system-bath interactions. The operators B_μ are composed of one- and two-body terms, where i, j index the bath qubits, $\mu, \alpha, \beta \in \{1, x, y, z\}$, where $\sigma^1 = I$ is the 2×2 identity matrix, and $c^\mu_{\alpha\beta} \in [0, 1]$ are coefficients chosen uniformly at random. Constructing B_μ in this manner permits general two- and three-body interactions between the system and the environment, and also facilitates a direct comparison with Ref. [26], where the same model was used.

The single-axis error $E_\mu(\tau)$ will be dominated by the lowest non-vanishing order of τ, which we denote by n_μ. I.e., $E_\mu \sim \mathcal{O}(\tau^{n_\mu})$ provided the first $n_\mu - 1$ terms of the power series expansion of $B''_\mu(\tau)$ vanish. More expliclity, we write

$$B''_\mu(\tau) = \sum_{j=n_\mu}^{\infty} B''^{(j)}_\mu \tau^j, \tag{29}$$

where

$$B''^{(j)}_\mu = \sum_{\vec{\alpha}^\mu_j} r^\mu_{\alpha_1\alpha_2\ldots\alpha_j}\ B_{\alpha_1} B_{\alpha_2} \cdots B_{\alpha_j}, \tag{30}$$

and where $\vec{\alpha}^\mu_j = \{\alpha_1, ..., \alpha_j\}$ such that $\alpha_j \in \{1, x, y, z\}$ and $\mu = \prod_j \alpha_j$, with the Pauli product rules $xy = z, zx = y, yz = x$. In this manner we have a convenient notation to identify the environment operators present in each single-axis error. For example, if $E_z(\tau) \sim \mathcal{O}(\tau^2)$ then the possible summands comprising $B''^{(2)}_z$ will be proportional to $B_0 B_z$, $B_z B_0$, $B_x B_y$, and $B_y B_x$. The constituent operators, B_{α_j}, are the environment operators initially defined in Eq. (4). The only terms of interest are those proportional to τ^{n_μ}, since these are the dominant terms of $B''_\mu(\tau)$. Using Eqs. (22), (29) and (30), and the submultiplicativity property of unitarily invariant norms [37], the single-axis error is

$$\begin{aligned} E_\mu(\tau) &\sim \|B''^{(n_\mu)}_\mu \tau^{n_\mu}\|_F \\ &\leq \tau^{n_\mu} \sum_{\vec{\alpha}^\mu_{n_\mu}} |r^\mu_{\alpha_1\ldots\alpha_{n_\mu}}| \|B_{\alpha_1}\|_F \cdots \|B_{\alpha_{n_\mu}}\|_F \\ &= \tau^{n_\mu} \sum_{\vec{\alpha}^\mu_{n_\mu}} \tilde{r}^\mu_{\alpha_1\ldots\alpha_{n_\mu}} J_{\alpha_1} \cdots J_{\alpha_{n_\mu}}, \end{aligned} \tag{31}$$

where we have only kept the leading order contribution in τ. The coupling strength parameters defined in Eq. (26) have been incorporated into the sum, such that $J_1 = \beta$ and $J_{x,y,z} \leq J$. The parameters $\tilde{r}^\mu_{\alpha_1\alpha_2\ldots\alpha_{n_\mu}}$ account for a conversion factor between the Frobenius and sup-operator norms. Note that the reason we chose to work with the Frobenius norm is that the distance measure (25) is expressed in terms of this norm. Factoring J^{n_μ} out from the sum, the desired functional form of the single-axis error is

$$\log(E_\mu) \sim n_\mu \log(J\tau) + \log\left(\chi^\mu\right), \tag{32}$$

with

$$\chi^\mu = \sum_{\vec{\alpha}^\mu_{n_\mu}} \tilde{r}^\mu_{\alpha_1\alpha_2\ldots\alpha_{n_\mu}}\ \gamma_{\alpha_1}\gamma_{\alpha_2}\cdots\gamma_{\alpha_{n_\mu}}, \tag{33}$$

and with

$$\gamma_\alpha = J_\alpha / J \leq 1. \tag{34}$$

We have written the single-axis error as Eq. (32) in anticipation of our numerical results, where we plot E_μ as a function of the dimensionless parameter $J\tau$. In the $\beta \ll J$ regime it is J which sets the relevant bath timesale and hence we expect that $J\tau \lesssim 1$ should be a necessary condition for DD to be beneficial over uncontrolled free evolution, and we shall see that our simulations support this expectation. The quantity χ_μ does not depend on τ and hence will play the role of a constant offset. In the next section we shall unravel the connection between the suppression order n_μ and the sequence orders N_1 and N_2.

V. NUMERICAL RESULTS

We now present a numerical analysis of QDD based on the single-axis errors and the overall distance measure $D(U, G)$. The initial focus is the single-axis error, which we use to quantify the decoherence suppression as a function of inner and outer sequence orders.

A. Single-axis errors

Figures 1 and 2 display the single-axis errors as a function of $J\tau$ for $N_2 = 3$ and $N_2 = 4$, respectively, with the inner sequence order varying from $N_1 = 1$ to $N_1 = 10$. The pure bath and system-bath interaction strengths were adjusted such that the Hamiltonian is dominated by the interaction, $\beta \ll J$. Each data point corresponds to a single cycle of the QDD sequence averaged over 50 random instances of the parameters $c^\mu_{\alpha\beta}$ appearing in Eq. (28). Since we keep the minimum pulse interval fixed, the total sequence duration increases with increasing N_1 and N_2. The first thing to notice about Figures (1) and (2) is that they match the prediction of Eq. (32) very well in the regime of small $J\tau$. Namely, in all cases we observe a constant slope, until $J\tau \sim \mathcal{O}(1)$. This is also in agreement with the result of Ref. [26].

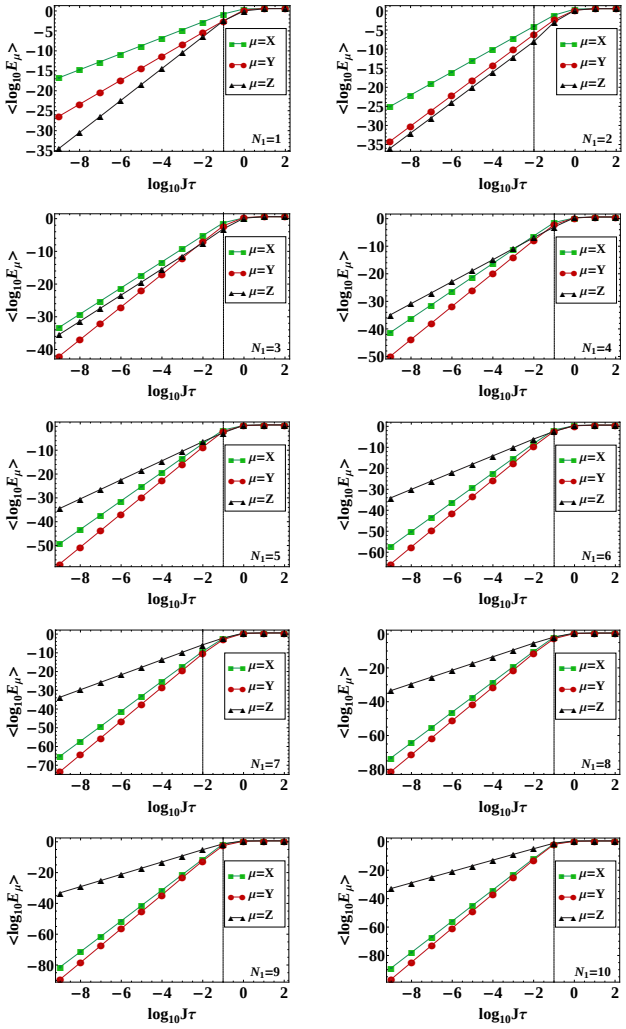

FIG. 1: (color online) Single-axis errors after one cycle of $U_\Omega^{(N_1,N_2)}$ for outer sequence order $N_2 = 3$ and inner sequence orders $N_1 = 1, 2, \ldots, 10$ as a function of $J\tau$, averaged over 50 random realizations of the bath operators B_μ. Error bars are shown but are very small. In all our simulations we set $J = 10^{-4}$ and $\beta = 10^{-6}$. Single-axis error values were computed for $\log_{10}(J\tau) = -9, -8, \ldots, 2$. Lines are guides to the eye. E_x is designated by the green squares, E_y by the red circles, and E_z by the black triangles. Note that $\log_{10}(E_z)$ is the same in all six plots, with a slope of $N_2 + 1$. The slope of $\log_{10}(E_x)$, on the other hand, is $N_1 + 1$. The slope of $\log_{10}(E_y)$ is $N_1 + 2$. Vertical lines denote the largest value of $J\tau$ utilized in the linear regression used to extract the slope n_μ.

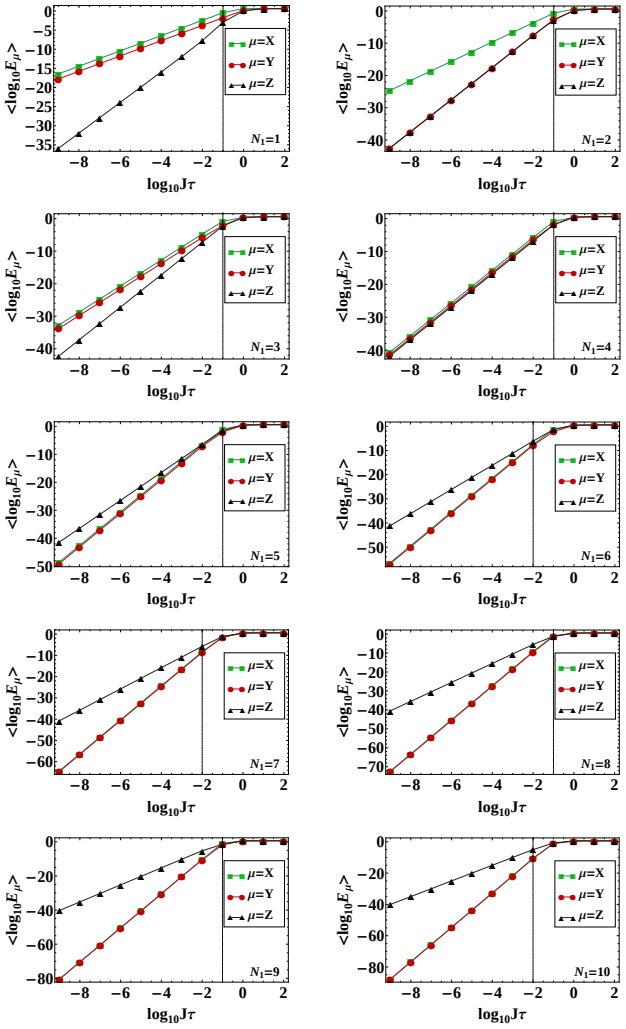

FIG. 2: (color online) Single-axis errors after one cycle of $U_\Omega^{(N_1,N_2)}$ for outer sequence order $N_2 = 4$ and inner sequence orders $N_1 = 1, 2, \ldots, 10$ (left to right, top to bottom) as a function of $J\tau$, averaged over 50 random realizations of the bath operators B_μ. Other details as in Fig. 1, except that the single-axis error suppressed by both the inner and outer sequence, $E_y(\tau)$, exhibits a strong dependence on the parity of the inner sequence. Note that for each value of N_1, $E_x(\tau)$ and $E_y(\tau)$ are essentially equal for all values of $J\tau$.

A summary of the scalings for $E_\mu(J\tau)$ are given in Table I for all combinations of $N_1, N_2 \in \{1, 2, \ldots, 10\}$. The values of n_μ were extracted by performing linear regressions for $\log_{10}[E_\mu(J\tau)]$ between $\log_{10}(J\tau) = -9$ and the values of $\log_{10}(J\tau)$ indicated by the vertical lines in Figs. 1 and 2, and rounding to the nearest integer (in all cases the deviation from an integer value was at most in the third significant digit). We shall return to Table I after presenting and discussing the data in the figures.

Let us then consider in detail the effect of varying the inner and outer sequence orders on the single-axis errors. When $N_2 > N_1$, higher order suppression is expected for the errors that correspond to the system basis operators which anticommute with the member of the MOOS comprising the outer X-type sequence. Thus the single-axis errors $E_y(\tau)$ and $E_z(\tau)$ are most heavily suppressed.

Since only the outer sequence can suppress z-axis, or Z-type errors [recall Eq. (5)], $E_z(J\tau)$ only gains additional error suppression if the outer sequence order is increased. In Fig. (1), $N_2 = 3$ and $E_z(J\tau) \sim \mathcal{O}[(J\tau)^4]$ for all N_1, exhibiting error suppression of the first N_2 terms of the interactions proportional to σ^z. Thus QDD operates with UDD efficiency for error suppression by the outer nested sequence alone.

In a similar manner to $E_z(J\tau)$, the behavior of $E_x(J\tau)$ can be attributed to one of the two nested sequences. Namely,

the error measured by E_x is associated with σ^x, which only anti-commutes with the MOOS operator present in the inner Z-type sequence. Determined solely by the inner sequence order, $E_x(J\tau) \sim \mathcal{O}[(J\tau)^{N_1+1}]$. Essentially, the outer sequence has no effect on the order of error suppression for $E_x(J\tau)$, as can be seen from Fig. 1 for $N_2 = 3$.

The interpretation for $E_y(J\tau)$ is not as simple, since this single-axis error is compensated by both the inner and outer sequences. One might expect both the inner and outer sequence to contribute to Y-type error suppression, i.e., $E_y(J\tau)$ to scale with $(J\tau)^{\max(N_1,N_2)+1}$. However, if this were the case then, e.g., the case $N_1 = 1$ would display an equal order of error suppression for both $E_y(\tau)$ and $E_z(\tau)$. Instead we find that $E_y(J\tau) \sim \mathcal{O}[(J\tau)^{N_1+2}]$ for $N_2 = 3$. Thus the suppression of $E_y(J\tau)$ is constrained by N_1, even when $N_2 > N_1$, though it is larger by one order of magnitude than UDD error suppression efficiency for the inner sequence.

Similar observations apply for all *odd*-order outer sequences we have analyzed (see Appendix A, Figures 7 9, 11, and 13). Odd-order sequences are anti-symmetric with respect to time-reversal, and the conclusions concerning the case $N_2 = 3$ can be generalized as follows: when the outer sequence is anti-symmetric, terms in the QDD evolution operator which anti-commute with only one element of the MOOS are suppressed with UDD efficiency, determined by the order of the nested sequence composed of the corresponding anti-commuting MOOS operator (this applies to σ^x and σ^z). In contrast, terma that anti-commutes with *both* elements of the MOOS are suppressed to one order beyond UDD efficiency, dictated exclusively by the inner sequence order (this applies to σ^y). Below we will see how this observation is modified when we consider larger values of N_2.

Comparing the case of the anti-symmetric outer sequence of Fig. 1 to that of the symmetric sequence of $N_2 = 4$ in Fig. 2, one notices immediately that there is a qualitative difference. The single-axis error $E_y(J\tau)$, the component anti-commuting with both the inner and outer sequences, σ^y, fluctuates strongly as a function of N_1. A similar effect is observed for other even values of N_2 (see Appendix A, Figures 8, 10, 12, and 14). Only the outer sequence order has been changed, therefore this characteristic is entirely dependent on the fact that the outer sequence is now symmetric.

Analogous to the anti-symmetric outer sequence, Fig. 2 shows that the single-axis error $E_z(J\tau)$ is independent of the inner sequence order. The scaling $E_z(J\tau) \sim \mathcal{O}[(J\tau)^5]$ holds for all N_1. Thus the single-axis error $E_z(J\tau)$ again exhibits UDD efficiency, independent of the parity of the outer sequence. Similarly, again $E_x(J\tau) \sim \mathcal{O}[(J\tau)^{N_1+1}]$ in Fig. 2.

However, when we consider the n_z results for all values of N_1 and N_2 we find that there are exceptions to this simple behavior. As can be seen from Table I, when $N_1 = 1$ and $N_2 \geq 4$, the value of n_z is fixed at 4. The same phenomenon is observed for $N_1 = 3$ and $N_2 \geq 8$.

On the basis of our numerical data we can summarize the scaling of the X and Z-type single-axis errors as follows:

$$n_x \;=\; N_1 + 1, \tag{35}$$

and

$$n_z = \begin{cases} N_2 + 1 & : N_1 \text{ even} \\ N_2 + 1 & : N_1 \text{ odd},\ N_2 < 2N_1 + 2 \\ 2N_1 + 2 & : N_1 \text{ odd},\ N_2 \geq 2N_1 + 2 \end{cases} \tag{36}$$

Qualitatively, we expect that when the inner sequence works imperfectly, as is the case for N_1 odd, the lowest order sequence will determine the scaling of the single axis error, and this is what is stated in Eq. (36).

As is clear from Fig. (2), the scaling of $E_y(J\tau)$ is dependent on the parity of N_1. If the inner sequence is of odd parity then $E_y(J\tau) \sim \mathcal{O}[(J\tau)^{N_1+2}]$ when N_2 is odd as well, or $E_y(J\tau) \sim \mathcal{O}[(J\tau)^{N_1+1}]$ when N_2 is even. Thus the scaling of E_y is dominated by the inner sequence order when N_1 is odd. The situation changes when N_1 is even. Now, if N_2 is odd the sequence is still anti-symmetric, however there is an immediate improvement in error suppression, $E_y(J\tau) \sim \mathcal{O}[(J\tau)^{\max(N_1+1,N_2)+1}]$. If the complete sequence is fully symmetric (both N_1 and N_2 even) we also find a scaling dependent on both the inner and outer sequence orders, $E_y(J\tau) \sim \mathcal{O}[(J\tau)^{\max(N_1,N_2)+1}]$. We thus see that the suppression of interactions which anti-commute with *both* elements of the MOOS depends sensitively on the parity of the inner sequence order, and is summarized for $E_y(J\tau) \sim \mathcal{O}[(J\tau)^{n_y}]$ as

$$n_y = \begin{cases} \max(N_1, N_2) + 1 & : N_1 \text{ even},\ N_2 \text{ even} \\ \max(N_1 + 1, N_2) + 1 & : N_1 \text{ even},\ N_2 \text{ odd} \\ N_1 + 1 & : N_1 \text{ odd},\ N_2 \text{ even} \\ N_1 + 2 & : N_1 \text{ odd},\ N_2 \text{ odd} \end{cases} \tag{37}$$

The dependence upon the symmetry of the inner sequence, the parity of N_1, was first noted by Wang & Liu in the context of overall QDD performance [27]. The dependence on the outer sequence symmetry, however, was not noted previously. Our results show that the symmetry of the outer sequence impacts the efficiency of σ^y error suppression as well.

The efficiency of QDD error suppression is directly related to the efficiency of UDD. Each interaction that anti-commutes with at least one member of the MOOS is expected to achieve UDD efficiency. Fully symmetric QDD, i.e., even order N_1 and N_2, recovers the efficiency of UDD for all single-axis errors. Consequently, QDD performs with optimal efficiency when it is fully symmetric.

The interactions addressed only by the inner or outer sequence are separately suppressed with UDD efficiency corresponding to the order of the corresponding sequence performing the decoherence suppression. Equivalently, interactions which anti-commute with only one member of the MOOS are suppressed with UDD efficiency in the QDD scheme. On the other hand, error suppression of the interactions anti-commuting with both elements of the MOOS is dependent upon the parity of both the inner and outer sequence orders.

(a) $n_x = N_1 + 1$ for $N_1, N_2 \in \{1, \ldots, 10\}$

(b)

	n_y									
N_1	$N_2=1$	$N_2=2$	$N_2=3$	$N_2=4$	$N_2=5$	$N_2=6$	$N_2=7$	$N_2=8$	$N_2=9$	$N_2=10$
1	3	2	3	2	3	2	3	2	3	2
2	4	3	4	5	6	7	8	9	10	11
3	5	4	5	4	5	4	5	4	5	4
4	6	5	6	5	6	7	8	9	10	11
5	7	6	7	6	7	6	7	6	7	6
6	8	7	8	7	8	7	8	9	10	11
7	9	8	9	8	9	8	9	8	9	8
8	10	9	10	9	10	9	10	9	10	11
9	11	10	11	10	11	10	11	10	11	10
10	12	11	12	11	12	11	12	11	12	11

(c)

	n_z									
N_1	$N_2=1$	$N_2=2$	$N_2=3$	$N_2=4$	$N_2=5$	$N_2=6$	$N_2=7$	$N_2=8$	$N_2=9$	$N_2=10$
1	2	3	4	4	4	4	4	4	4	4
2	2	3	4	5	6	7	8	9	10	11
3	2	3	4	5	6	7	8	8	8	8
4	2	3	4	5	6	7	8	9	10	11
5	2	3	4	5	6	7	8	9	10	11
6	2	3	4	5	6	7	8	9	10	11
7	2	3	4	5	6	7	8	9	10	11
8	2	3	4	5	6	7	8	9	10	11
9	2	3	4	5	6	7	8	9	10	11
10	2	3	4	5	6	7	8	9	10	11

TABLE I: Summary of the scaling for all single-axis errors. Values of n_μ were extracted by performing a linear regression, rounded to the nearest integer, fitting the slopes of the straight line portions of the curves displayed in Figs. 1 and 2, and the additional Figs. 7-10 in Appendix A, between $\log_{10}(J\tau) = -9$ and the values of $\log_{10}(J\tau)$ indicated by the vertical lines in these figures. (a) E_x, (b) E_y, and (c) E_z for $N_1, N_2 \in \{1, 2, \ldots, 10\}$. For n_y and n_z the outer sequence order N_2 is displayed in the top row and the inner sequence order N_1 in the first column. Each of the single-axis errors is dominated by the lowest order of $J\tau$, denoted n_μ, therefore $E_\mu \sim \mathcal{O}[(J\tau)^{n_\mu}]$. Additional simulations (not shown) fully continue the trends seen in this table and summarized in Eqs. (35)-(37) all the way up to $N_1, N_2 \leq 24$.

B. Intermediate single-axis errors

Rather than consider the single-axis errors just at the end of the QDD sequence, here we consider the single-axis errors prior to the application of each X-type outer sequence pulse. We will refer to these as "intermediate single-axis errors" since they are extracted during the QDD evolution, unlike those presented in Figures 1, 2, and 7-14 which are extracted at the end of the complete evolution. y studying this intermediate time-dependence of the errors we shall gain another interesting perspective on the manner in which the QDD sequence suppresses decoherence.

Let us define a set of "intermediate QDD" sequences as

$$\tilde{U}_\Omega^{(N_1,j)} \equiv Z^{(N_1)}(s_j\tau)XZ^{(N_1)}(s_{j-1}\tau)\cdots XZ^{(N_1)}(s_1\tau), \tag{38}$$

where $j \in \{1, \ldots, N_2 + 1\}$. Thus, except for $j = 1$, $\tilde{U}_\Omega^{(N_1,j)}$ contains $j - 1$ X-type pulses sandwiched between j Z-type UDD sequences. When $j = 1$

$$\tilde{U}_\Omega^{(N_1,1)} \equiv Z^{(N_1)}(s_1\tau) \tag{39}$$

is just the UDD sequence. We also separately define

$$\tilde{U}_\Omega^{(N_1,N_2+2)} \equiv U_\Omega^{(N_1,N_2)} = X^{N_2}\tilde{U}_\Omega^{(N_1,N_2+1)}, \tag{40}$$

i.e., the complete QDD sequence, Eq. (5). Note that $\tilde{U}_\Omega^{(N_1,N_2+2)}$ contains a final X pulse if N_2 is odd, but not if N_2 is even. Similarly to the error expansion (21), we have the intermediate error expansion

$$\tilde{U}_\Omega^{(N_1,j)} = B_I^{(j)}(\tau) + \sum_{\mu\in\{x,y,z\}} \sigma^\mu \otimes B_\mu^{(j)}(\tau). \tag{41}$$

In analogy to Eq. (22) we can now define the intermediate single-axis errors as

$$E_\mu^{(j)}(\tau) = \|B_\mu^{(j)}(\tau)\|_F, \tag{42}$$

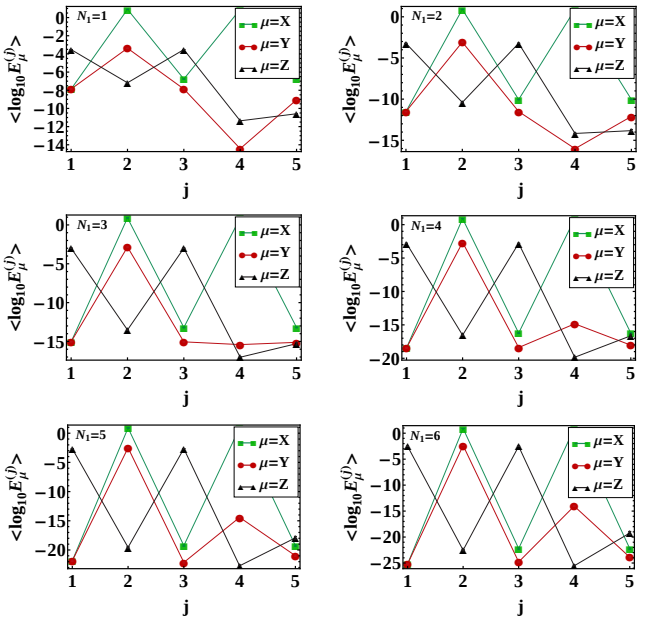

FIG. 3: (color online) Intermediate single-axis errors for $N_2 = 3$, as defined in Eq. (42). For given j, the intermediate single-axis error is computed after j innner Z-type UDD sequences separated by $j-1$ pulses. There are N_2+1 inner UDD sequences. The point $j=5$ is the last X pulse at the end of last inner UDD sequence, as required for odd N_2. Note that because the data points labeled $j=4$ and $j=5$ are separated by a single X pulse, and our pulses are instantaneous, these points have no actual time delay between them.

where $j \in \{1, N_2+2\}$. Note that for odd N_2 the errors $E_\mu^{(N_2+1)}$ and $E_\mu^{(N_2+2)}$ differ by a single instantaneous X pulse (which is significant, as our simulations results will demonstrate), while for N_2 even $E_\mu^{(N_2+1)} = E_\mu^{(N_2+2)}$, so that below we do not plot $E_\mu^{(N_2+2)}$ in the even case.

Figures 3 and 4 display the intermediate single-axis errors for $N_2 = 3$ and $N_2 = 4$, respectively, with $N_1 = 1, 2, \ldots, 6$. The coupling parameters are fixed at $J = 10^{-4}$ and $\beta = 10^{-6}$ as in the previous figures. Additional results for odd N_2 are given in Appendix A in Figures 19 and 21, and for even N_2 in Appendix A in Figures 20 and 22.

Several features are noteworthy in these figures.

(i) $E_x^{(1)}$ and $E_y^{(1)}$ are equal and substantially smaller than $E_z^{(1)}$, and the difference grows as N_1 is increased. This is because the inner Z-type sequence only suppresses the X and Y-type errors, and the point $j=1$ does not include the first X-type outer sequence pulse. Formally, this is expressed by

$$\begin{aligned} E_\mu^{(1)}(\tau) &= \|B_\mu^{(1)}\|_F \sim (s_1\tau)^{N_1+1}, \quad \mu \in \{x,y\} \\ E_\nu^{(1)}(\tau) &= \|B_\nu^{(1)}\|_F \sim 1, \quad \nu \in \{I,z\}. \end{aligned} \tag{43}$$

(ii) The intermediate single-axis errors all fluctuate throughout the QDD evolution. This is due to a reshuffling of the errors after each outer sequence X-type pulse is applied, a simple consequence of the rules of Pauli matrix multiplication. To see why in some detail, consider the effect of the first $X \equiv \sigma^x \otimes I$ pulse:

$$\begin{aligned} X\tilde{U}_\Omega^{(N_1,1)} &= \sigma^x \otimes B_I^{(1)} + \sum_{\nu\in\{x,y,z\}} \sigma^x\sigma^\nu \otimes B_\nu^{(1)} \\ &= B_x^{(1)} + \sigma^x \otimes B_I^{(1)} + \sigma^y \otimes B_z^{(1)} + \sigma^z \otimes B_y^{(1)}, \end{aligned} \tag{44}$$

where we dropped factors of i. The reshuffling effect is clear: for example, the error single-axis z-type error now comes from $B_y^{(1)}$. To explain the $j=2$ behavior we should consider the effect of multiplying $X\tilde{U}_\Omega^{(N_1,1)}$ by the next inner UDD sequence $Z^{(N_1)}(s_2\tau)$. The ith inner UDD sequence has the expansion

$$Z^{(N_1)}(s_i\tau) = B_{I,i} + \sigma^x \otimes B_{x,i} + \sigma^y \otimes B_{y,i} + \sigma^z \otimes B_{z,i}, \tag{45}$$

where similarly to Eq. (43) we have

$$\begin{aligned} \|B_{\mu,i}\|_F &\sim (s_i\tau)^{N_1+1}, \quad \mu \in \{x,y\} \\ \|B_{\nu,i}\|_F &\sim 1, \quad \nu \in \{I,z\}. \end{aligned} \tag{46}$$

Using this to carry out the multiplication to the next order we have

$$\begin{aligned} \tilde{U}_\Omega^{(N_1,2)} &= Z^{(N_1)}(s_2\tau)X\tilde{U}_\Omega^{(N_1,1)} \\ &= [B_{I,2} + \sigma^x \otimes B_{x,2} + \sigma^y \otimes B_{y,2} + \sigma^z \otimes B_{z,2}] \\ &\times [B_x^{(1)} + \sigma^x \otimes B_I^{(1)} + \sigma^y \otimes B_z^{(1)} + \sigma^z \otimes B_y^{(1)}] \end{aligned} \tag{47}$$

Consequently

$$\begin{aligned} E_x^{(2)}(\tau) &= \|B_{I,2}B_I^{(1)} + B_{x,2}B_x^{(1)} + B_{y,2}B_y^{(1)} + B_{z,2}B_z^{(1)}\|_F \\ &\sim 1 \\ E_y^{(2)}(\tau) &= \|B_{I,2}B_z^{(1)} + B_{x,2}B_y^{(1)} + B_{y,2}B_x^{(1)} + B_{z,2}B_I^{(1)}\|_F \\ &\sim 1 \\ E_z^{(2)}(\tau) &= \|B_{I,2}B_y^{(1)} + B_{x,2}B_z^{(1)} + B_{y,2}B_I^{(1)} + B_{z,2}B_x^{(1)}\|_F \\ &\sim 2(s_1\tau)^{N_1+1} + 2(s_2\tau)^{N_1+1}, \end{aligned} \tag{48}$$

where $E_x^{(2)}(\tau)$ is dominated by $B_{I,2}B_I^{(1)}$ and $E_y^{(2)}(\tau)$ is dominated by $B_{I,2}B_z^{(1)}$, neither of which is suppressed, whence the ~ 1 result. On the other hand every one of the terms in $E_z^{(2)}(\tau)$ is suppressed. Hence, as can be seen in Figures 3 and 4 (and their companions, Figures 19-22 in the Appendix), at $j=2$ both the X and Y-type errors have increased relative to $j=1$, while the Z-type error has decreased. One can similarly understand the remaining oscillations of the intermediate single-axis errors in terms of this reshuffling of error types.

(iii) E_x and E_z oscillate out of phase, while E_y oscillates in phase with E_x for even N_2, but not necessarily for odd N_1. This is again a consequence of error reshuffling. The Y-type error behaves differently from the other two since it experiences suppression from both the inner and outer sequences. For the same reason we always find $E_y^{(j)} < E_x^{(j)}$.

(iv) E_x attains its minimum for $j=1$ and then slowly increases, though while maintaining its suppression *order*. This is because the X-type error is suppressed only by the inner

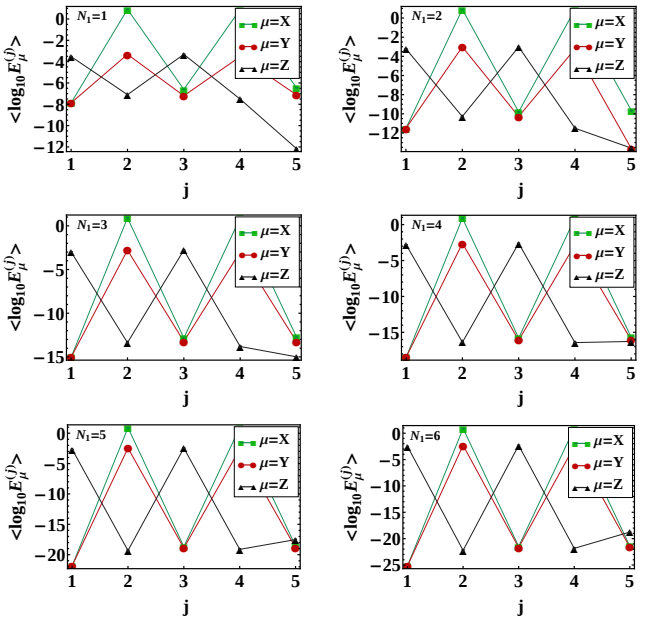

FIG. 4: (color online) Intermediate single-axis errors for $N_2 = 4$. As in Fig. 3 except that there is no final X pulse for N_2 even, i.e., there are $N_2 + 1$ inner UDD sequences separated by N_2 X pulses.

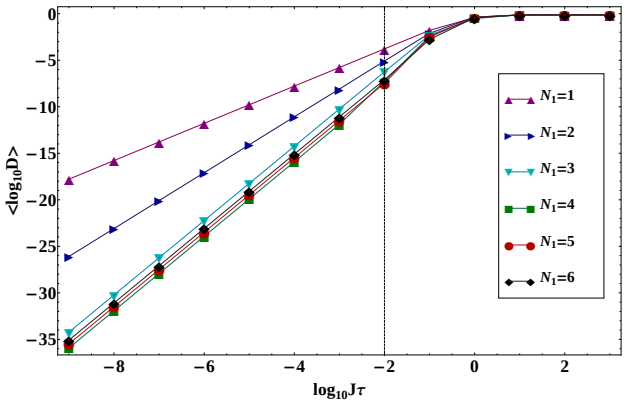

FIG. 5: (color online) Overall QDD distance measure after one cycle of $U_\Omega^{(N_1,N_2)}$ for outer sequence order $N_2 = 3$ and inner sequence orders $N_1 = 1, 2, \ldots, 6$, as a function of $J\tau$, averaged over 50 random realizations of the bath operators B_μ. The performance of QDD progressively improves with increasing N_1 up to $N_2 = N_1$, indicating that $\min\{N_1, N_2\}$ dominates QDD performance.

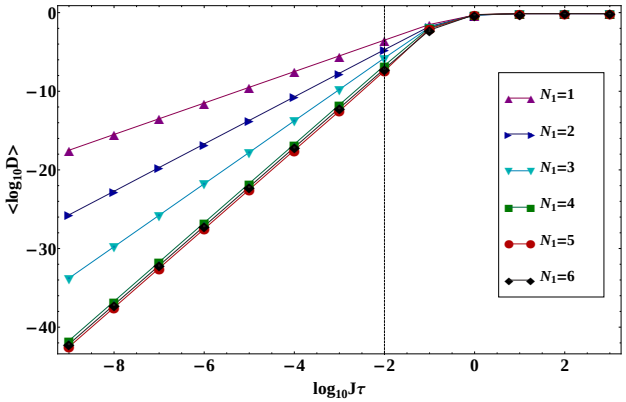

FIG. 6: (color online) Overall QDD distance measure after one cycle of $U_\Omega^{(N_1,N_2)}$ for outer sequence order $N_2 = 4$ and inner sequence orders $N_1 = 1, 2, \ldots, 6$, as a function of $J\tau$, averaged over 50 random realizations of the bath operators B_μ. The dependence of the order of error suppression on $\min\{N_1, N_2\}$ is again observed.

sequences, and these are simply applied to it with fixed order (N_1), a total of N_2 or $N_2 + 1$ times. Repeated application of the inner UDD sequence is similar to the periodic DD (PDD) protocol, whose performance is well known to deteriorate as time grows [12, 40]. The reason is that the error accumulates over time, without a mechanism for reducing it.

(v) There does not appear to be much of a difference between even and odd values of N_2 in terms of the intermediate single-axis errors. One difference is that $E_y^{(j)}$ tends to be more erratic for odd N_2 at high j values. We do not have a simple explanation for this behavior. Another difference is that for even N_2 all single-axis errors have the same final value when $N_1 = N_2$, but for odd N_2 the X-type error is always slightly worse at the end of the sequence, thus setting the bottleneck. Perhaps additional pulse interval optimization can remove this asymmetry.

(vi) Only at the very end are all three single-axis errors simultaneously small. Thus, while suppression of one error type can be achieved in the middle of the QDD sequence, one must wait until its completion to suppress all errors.

C. Overall performance

While the single-axis error analysis presented in the previuous two subsections helps in unravelling the mechanism of QDD performance, it does of course not tell the whole story. We now present our results for the distance measure $D(U, I)$ [Eq. (25)], which provides a complete quantitative description of QDD performance. We expect this overall performance of QDD to be dictated by the lowest order of τ present in the final evolution operator, Eq. (21), i.e.,

$$D \sim \mathcal{O}[(J\tau)^{n_D}] \tag{49}$$

where

$$n_D = \min(n_x, n_y, n_z). \tag{50}$$

Overall QDD performance for $N_2 = 3$ and $N_2 = 4$ is shown in Figures 5 and 6, respectively. The outer sequence order N_2 is fixed and the inner sequence order N_1 is varied from 1 to 6. These results are for the same model considered in the previous subsection. Additional results are given in Appendix A for $N_2 = 1, 2, 5, 6$ (see Figures 15-18). A summary of the distance scaling results is presented in Table II.

Considering $N_2 = 3$ first (Fig. 5), when $N_2 > N_1$ the overall order of error suppression is hindered by the inner

	n_D									
N_1	$N_2=1$	$N_2=2$	$N_2=3$	$N_2=4$	$N_2=5$	$N_2=6$	$N_2=7$	$N_2=8$	$N_2=9$	$N_2=10$
1	2	2	2	2	2	2	2	2	2	2
2	2	3	3	3	3	3	3	3	3	3
3	2	3	4	4	4	4	4	4	4	4
4	2	3	4	5	5	5	5	5	5	5
5	2	3	4	5	6	6	6	6	6	6
6	2	3	4	5	6	7	7	7	7	7
7	2	3	4	5	6	7	8	8	8	8
8	2	3	4	5	6	7	8	9	9	9
9	2	3	4	5	6	7	8	9	10	10
10	2	3	4	5	6	7	8	9	10	11

TABLE II: Summary of the scaling of the overall distance measure D with respect to inner and outer sequence orders, N_1 and N_2, respectively. Values of n_D were extracted by performing a linear regression, rounded to the nearest integer, fitting the slopes of the straight line portions of the curves displayed in Figs. 1 and 2 and the additional Figs. 15-18 in Appendix A between $\log(J\tau) = -9$ and the values of $\log(J\tau)$ indicated by the vertical lines in these figures. The outer sequence order N_2 is displayed in the top row and the inner sequence order N_1 in the first column. We find that, as expected, $n_D = \min(n_x, n_y, n_z)$. Additional simulations (not shown) fully continue the trends seen in this table and summarized in Eq. (50) all the way up to $N_1, N_2 \leq 24$.

sequence order. This is evident by the increasing order of error suppression as N_1 increases. In this regime the lower sequence order is determined by the inner sequence, therefore the scaling of D is equivalent to that of E_x, i.e., $D \sim \mathcal{O}[(J\tau)^{N_1+1}]$. As N_1 passes N_2, there is a saturation of error suppression corresponding to a performance bounded by the lower outer sequence order. The amplitude of performance increases slightly beyond $N_2 = N_1$, however begins to decrease when $N_1 > N_2$, as evidenced not by the slope but by the offset of the distance curves. Namely, the ordering, from worst to best, is $N_1 = 6, 5, 4$. The latter is an interesting feature not easily deduced from the single-axis errors. Increasing the inner sequence order results in an accumulation of error for the single-axis error dominating the performance; when $N_1 > N_2 + 1$ this corresponds to E_z.

The results are similar for $N_2 = 4$, as shown by Fig. 6. The order of error suppression, given by the slope, increases until $N_1 = N_2$ in correspondence with an overall performance dominated by the lowest order of τ present in E_μ. In addition to the saturation of the order of error suppression, we again observe an offset-related deterioration. Namely, $N_1 = 6$ is slightly worse than $N_1 = 5$.

VI. CONCLUSIONS

This work presents a comprehensive numerical analysis of the error suppression characteristics of QDD. This was achieved by isolating the single-axis errors associated with each system basis operator in the system-bath interaction. The order of error suppression was determined by computing the single-axis error as a function of the minimum pulse interval. We performed our analysis for a model in which the system-environment interaction dominated the internal bath dynamics, so that we could study the properties of the single-axis errors in the regime where DD is most beneficial. We constructed our QDD sequences with N_1 Z-type pulses comprising the inner sequence, and N_2 X-type pulses comprising the outer sequence. We found that the system-bath interaction term proportional to σ^x is suppressed with UDD efficiency for all values of N_1 and N_2 [Eq. (35)]. The interactions proportional to σ^z and σ^y both exhibit parity effects [Eqs. (36), (37)] whose origins are the symmetry or anti-symmetry of the inner and outer UDD sequences. Of course, permuting the pulse types of the inner and outer sequences will correspondingly modify these conclusions.

We also performed an analysis of the intermediate time-dependent performance of QDD. We found that the single-axis errors are strongly time-dependent, oscillating between outer-sequence pulses, until they all converge to nearly the same value after the final outer-sequence pulse. The closest convergence occurs for QDD sequences with equal inner and outer orders.

Finally, we computed the overall performance of QDD using an appropriate distance measure, and reconciled its scaling with that of the single-axis errors. We showed that overall QDD error suppression scales with the lowest order of single-axis error suppression, i.e., the first non-vanishing contribution appears at order $\min(N_1, N_2) + 1$. QDD accomplishes this by applying $(N_1 + 1)(N_2 + 1)$ pulses. We conjecture that similarly, for NUDD with K nested UDD sequences using $(N_1+1)(N_2+1)\cdots(N_K+1)$ pulses, the first non-vanishing contribution will appear at order $\min_j(N_j) + 1$.

In this work we treated the pulses as ideal, instantaneous operations. However, this is of course an idealization. An important topic for future study is robustness with respect to pulse errors, whether random or systematic. This topic has been addressed for UDD both theoretically [41, 42] and experimentally [43], and the overall conclusion is that pulse errors can have a dramatic negative impact unless they are compensated for. Some combination of pulse shaping and optimization will surely be required to overcome this problem in the

context of QDD as well.

Acknowledgments

We are grateful to Gonzalo Alvarez, Wan-Jung Kuo, Stefano Pasini, Dieter Suter, and Götz Uhrig for very helpful discussions. DAL acknowledges support from the U.S. Department of Defense and the NSF under Grants No. CHM-1037992 and CHM-924318.

[1] T. D. Ladd *et al.*, Nature **464**, 45 (2010).
[2] M. Schlosshauer, *Decoherence and the quantum-to-classical transition*, *The Frontiers Collection* (Springer, Berlin, 2007).
[3] L. Viola, E. Knill, and S. Lloyd, Phys. Rev. Lett. **82**, 2417 (1999).
[4] L. Viola and S. Lloyd, Phys. Rev. A **58**, 2733 (1998).
[5] L.-M. Duan and G. Guo, Phys. Lett. A **261**, 139 (1999).
[6] M. Ban, J. Mod. Optics **45**, 2315 (1998).
[7] P. Zanardi, Phys. Lett. A **258**, 77 (1999).
[8] F. Gaitan, *Quantum Error Correction and Fault Tolerant Quantum Computing* (CRC, Boca Raton, 2008).
[9] G. Gordon, G. Kurizki, and D. A. Lidar, Phys. Rev. Lett. **101**, 010403 (2008).
[10] J. Clausen, G. Bensky, and G. Kurizki, Phys. Rev. Lett. **104**, 040401 (2010).
[11] K. Khodjasteh and D. A. Lidar, Phys. Rev. Lett. **95**, 180501 (2005).
[12] K. Khodjasteh and D. A. Lidar, Phys. Rev. A **75**, 062310 (2007).
[13] H.-K. Ng, D. A. Lidar, and J. P. Preskill, Phys. Rev. A **84**, 012305 (2011).
[14] W. M. Witzel and S. Das Sarma, Phys. Rev. B **76**, 241303(R) (2007).
[15] W. Zhang *et al.*, Phys. Rev. B **75**, 201302 (2007).
[16] W. Zhang *et al.*, Phys. Rev. B **77**, 125336 (2008).
[17] J. R. West, D. A. Lidar, B. H. Fong, and M. F. Gyure, Phys. Rev. Lett. **105**, 230503 (2010).
[18] X. Peng, D. Suter, and D. Lidar, J. Phys. B, in press (2011).
[19] G. A. Álvarez, A. Ajoy, X. Peng, and D. Suter, Phys. Rev. A **82**, 042306 (2010).
[20] A. M. Tyryshkin *et al.*, (2010), eprint arXiv:1011.1903.
[21] Z. Wang *et al.*, (2010), eprint arXiv:1011.6417.
[22] C. Barthel *et al.*, (2010), eprint arXiv:1007.4255.
[23] G. Uhrig, Phys. Rev. Lett. **98**, 100504 (2007).
[24] W. Yang and R.-B. Liu, Phys. Rev. Lett. **101**, 180403 (2008).
[25] G. Uhrig, Phys. Rev. Lett. **102**, 120502 (2009).
[26] J. R. West, B. H. Fong, and D. A. Lidar, Phys. Rev. Lett. **104**, 130501 (2010).
[27] Z.-Y. Wang and R.-B. Liu, Phys. Rev. A **83**, 022306 (2011).
[28] M. Mukhtar, W. T. Soh, T. B. Saw, and J. Gong, Phys. Rev. A **82**, 052338 (2010).
[29] L. Jiang and A. Imambekov, (2011), eprint arXiv:1104.5021.
[30] J. R. Petta *et al.*, Science **309**, 2180 (2005).
[31] W. Yang and R.-B. Liu, Phys. Rev. Lett. **101**, 180403 (2008).
[32] G. Uhrig and D. Lidar, Phys. Rev. A **82**, 012301 (2010).
[33] K. Khodjasteh, T. Erdélyi, and L. Viola, Phys. Rev. A **83**, 020305 (2011).
[34] S. Pasini and G. S. Uhrig, J. Phys. A **43**, 132001 (2010).
[35] Z. Wang and R. Liu, (2011), eprint arXiv:1101.5286.
[36] W.-J. Kuo and D. Lidar, (2011), eprint arXiv:1106.2151.
[37] R. Bhatia, *Matrix Analysis*, No. 169 in *Graduate Texts in Mathematics* (Springer-Verlag, New York, 1997).
[38] M. D. Grace *et al.*, New J. Phys. **12**, 015001 (2010).
[39] M. Nielsen and I. Chuang, *Quantum Computation and Quantum Information* (Cambridge University Press, Cambridge, England, 2000).
[40] K. Khodjasteh and D. A. Lidar, Phys. Rev. A **78**, 012355 (2008).
[41] G. S. Uhrig and S. Pasini, New J. Phys. **12**, (2010).
[42] S. Pasini, P. Karbach, and G. S. Uhrig, (2010), eprint arXiv:1009.2638.
[43] A. Ajoy, G. A. Álvarez, and D. Suter, Phys. Rev. A **83**, 032303 (2011).

Appendix A: Additional Numerical Results

In this appendix we present additional figures in support of the numerical results presented in the body of the paper.

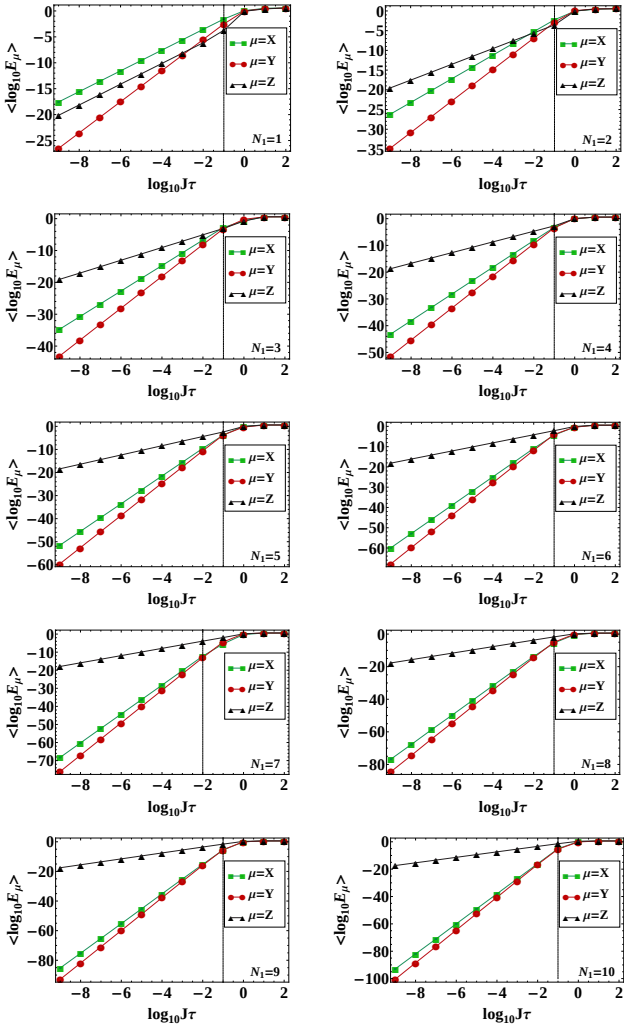

FIG. 7: (color online) Single-axis errors after one cycle for $N_2 = 1$ and $N_1 = 1, 2, \ldots, 10$ (left to right, top to bottom). See Fig. 1 for additional details.

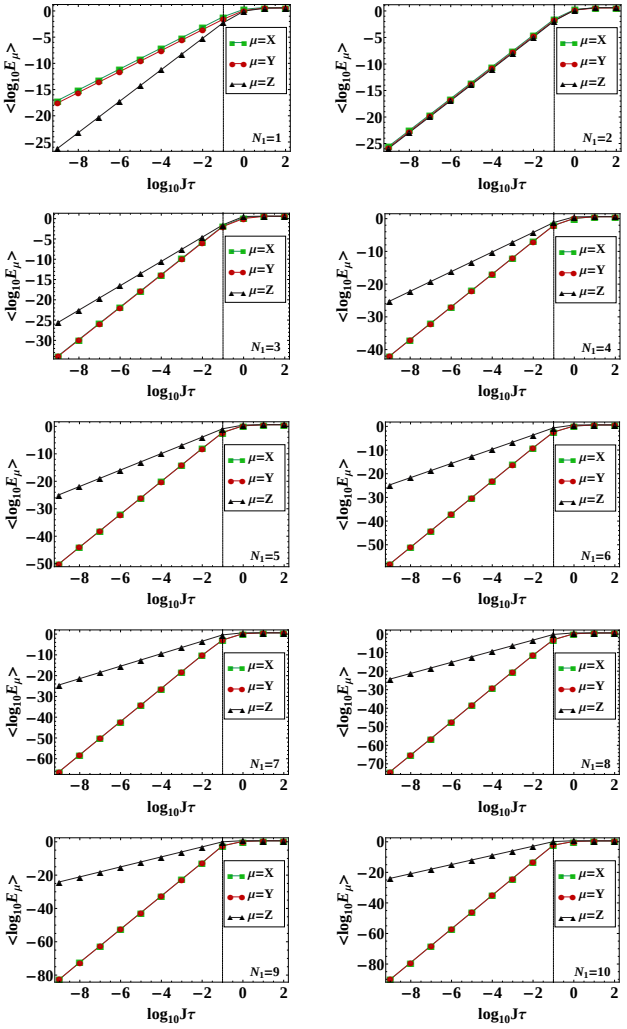

FIG. 8: (color online) Single-axis errors after one cycle for $N_2 = 2$ and $N_1 = 1, 2, \ldots, 10$ (left to right, top to bottom). See Fig. 2 for additional details.

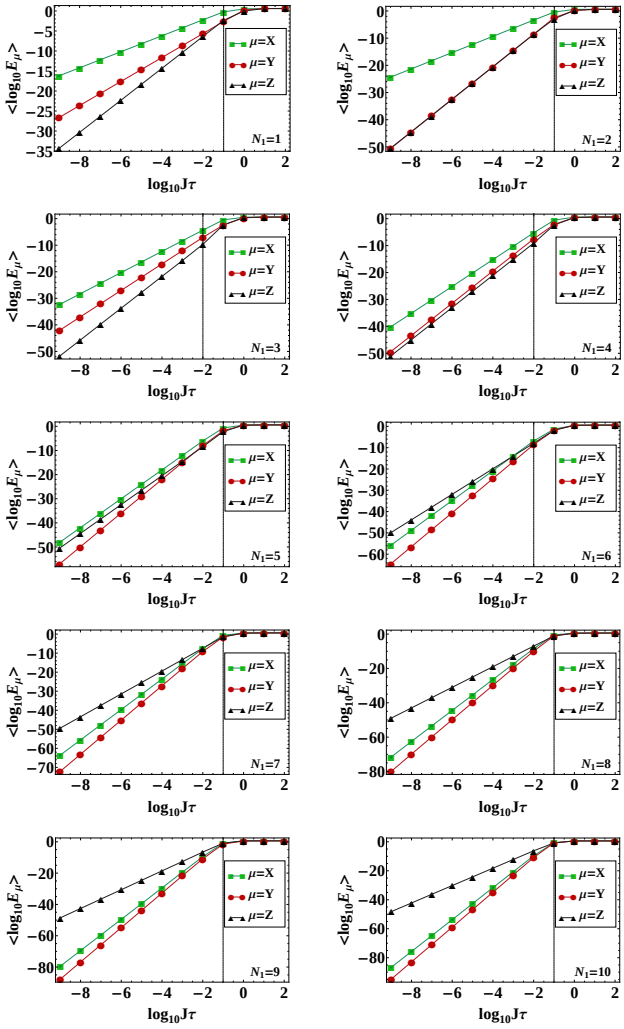

FIG. 9: (color online) Single-axis errors after one cycle for $N_2 = 5$ and $N_1 = 1, 2, \ldots, 10$ (left to right, top to bottom). See Fig. 1 for additional details.

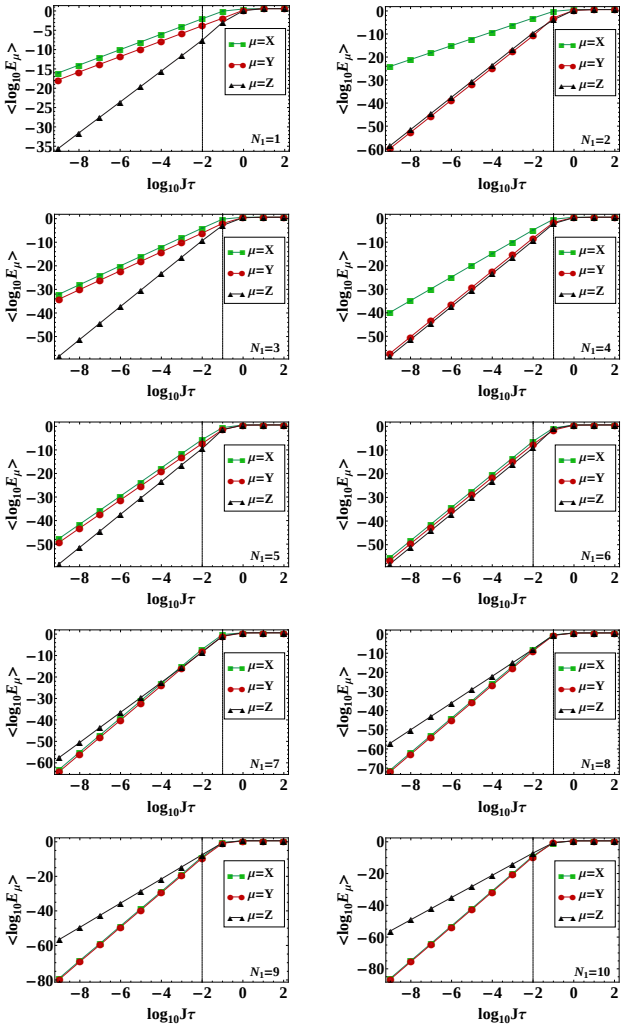

FIG. 10: (color online) Single-axis errors after one cycle for $N_2 = 6$ and $N_1 = 1, 2, \ldots, 10$ (left to right, top to bottom). See Fig. 2 for additional details.

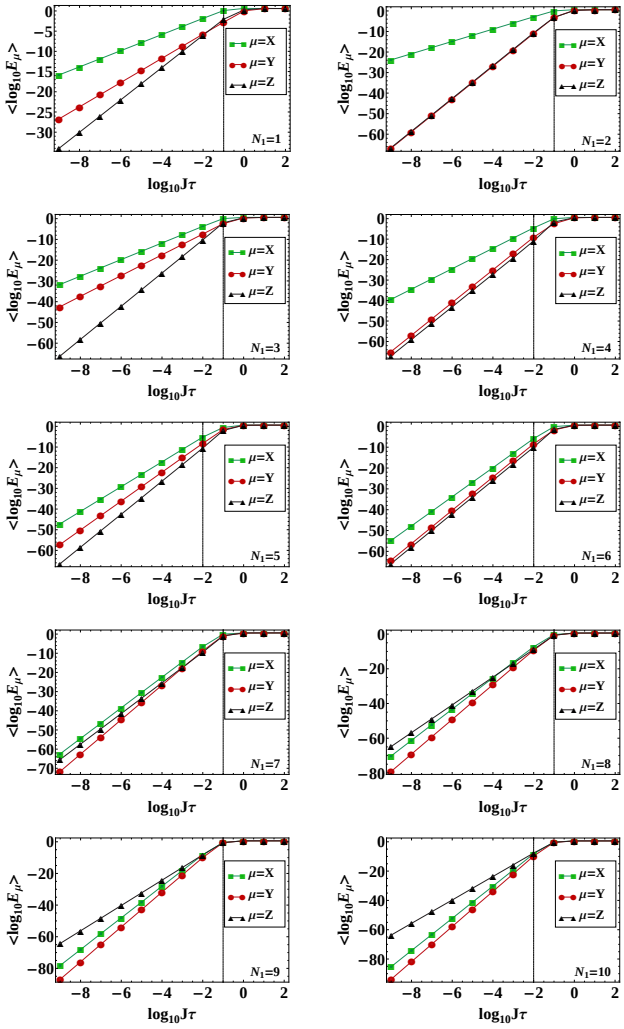

FIG. 11: (color online) Single-axis errors after one cycle for $N_2 = 7$ and $N_1 = 1, 2, \ldots, 10$ (left to right, top to bottom). See Fig. 2 for additional details.

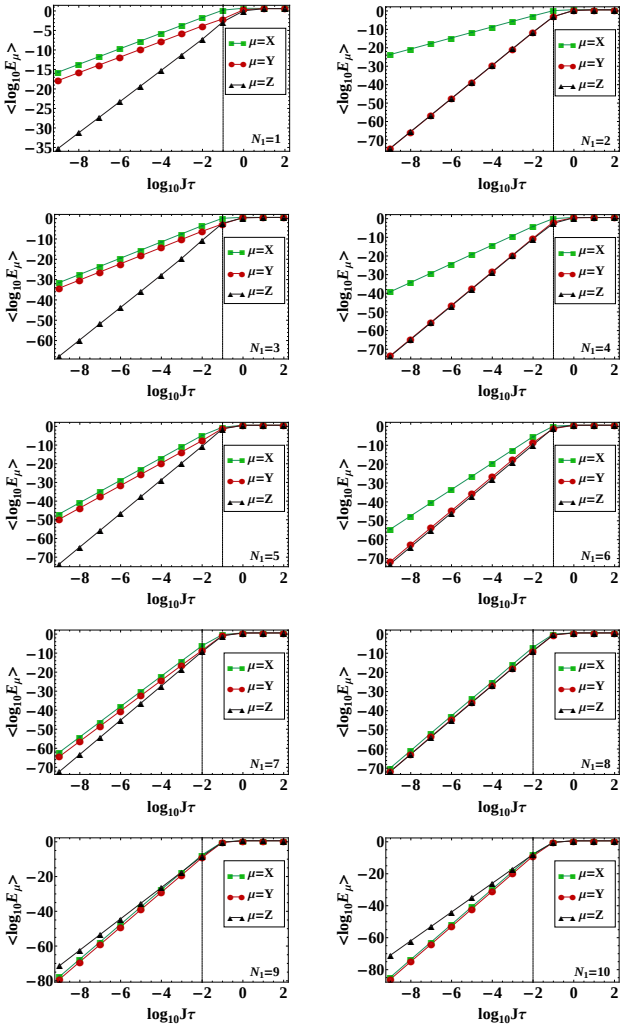

FIG. 12: (color online) Single-axis errors after one cycle for $N_2 = 8$ and $N_1 = 1, 2, \ldots, 10$ (left to right, top to bottom). See Fig. 2 for additional details.

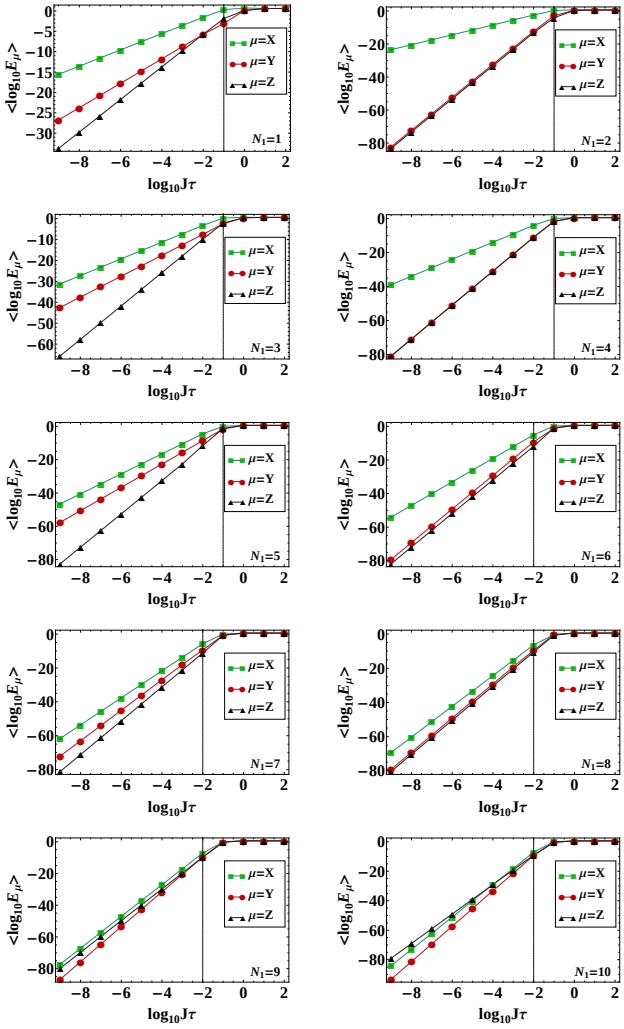

FIG. 13: (color online) Single-axis errors after one cycle for $N_2 = 9$ and $N_1 = 1, 2, \ldots, 10$ (left to right, top to bottom). See Fig. 2 for additional details.

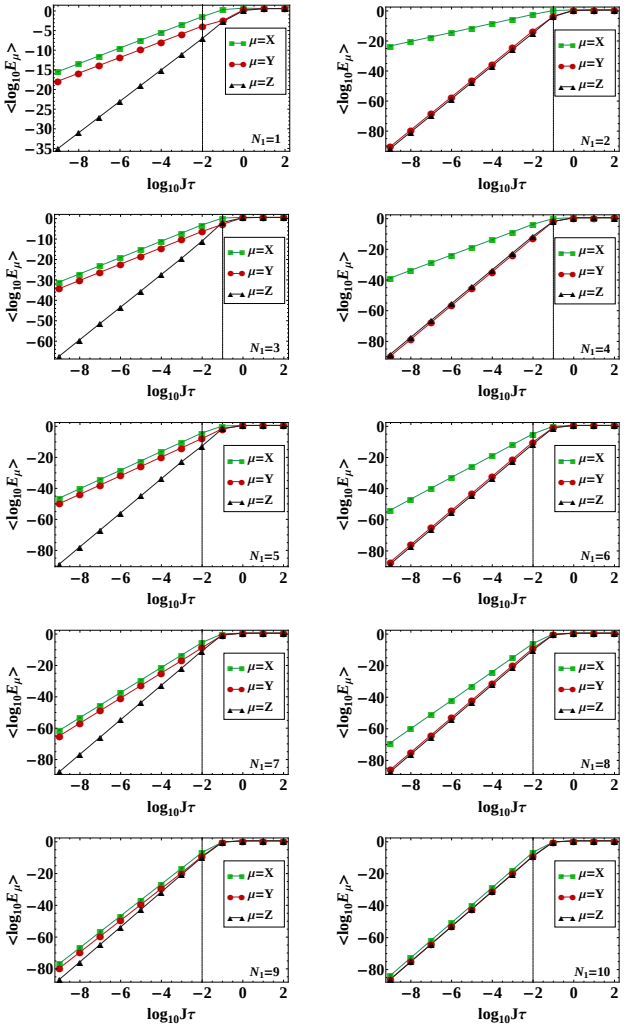

FIG. 14: (color online) Single-axis errors after one cycle for $N_2 = 10$ and $N_1 = 1, 2, \ldots, 10$ (left to right, top to bottom). See Fig. 2 for additional details.

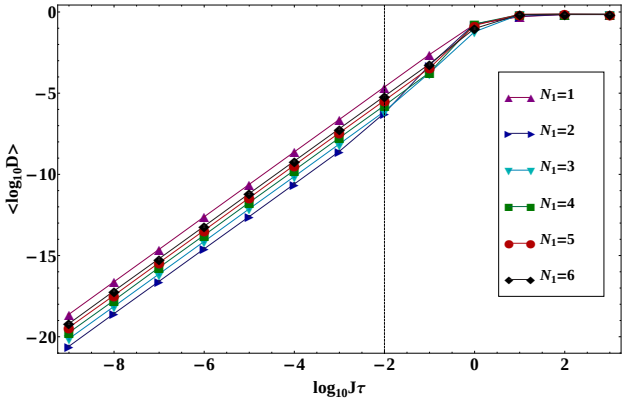

FIG. 15: (color online) Overall QDD distance measure after one cycle for $N_2 = 1$ and $N_1 = 1, 2, \ldots, 6$. See Fig. 5 for additional details.

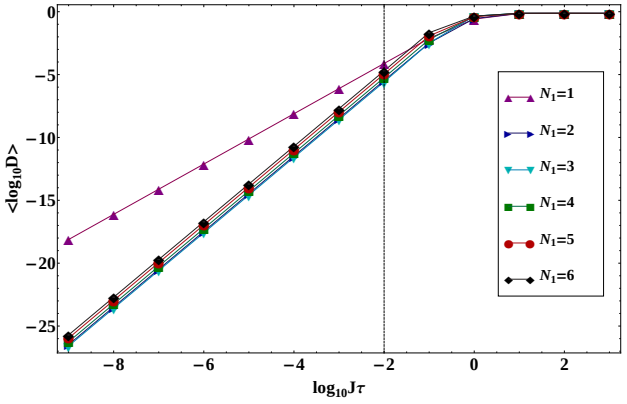

FIG. 16: (color online) Overall QDD distance measure after one cycle for $N_2 = 2$ and $N_1 = 1, 2, \ldots, 6$. See Fig. 6 for additional details.

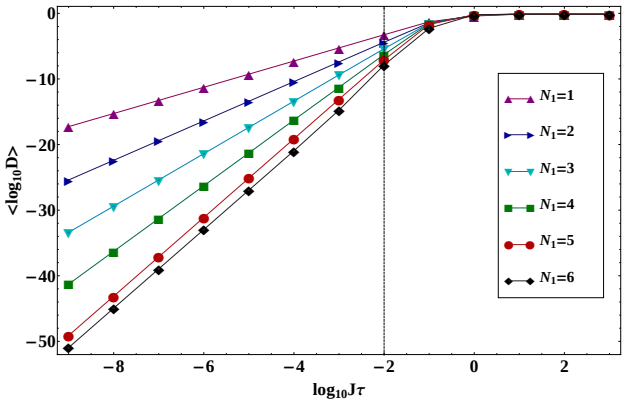

FIG. 17: (color online) Overall QDD distance measure after one cycle for $N_2 = 5$ and $N_1 = 1, 2, \ldots, 6$. See Fig. 5 for additional details.

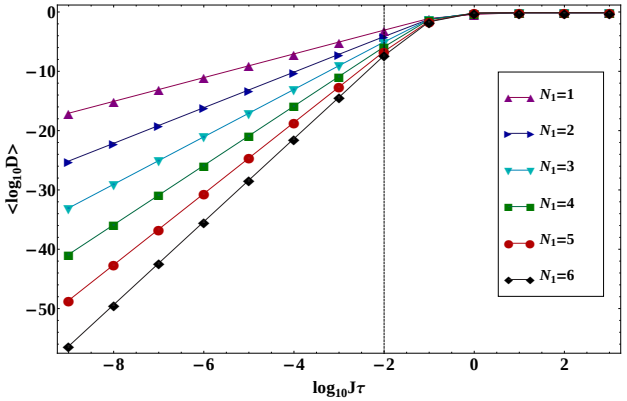

FIG. 18: (color online) Overall QDD distance measure after one cycle for $N_2 = 6$ and $N_1 = 1, 2, \ldots, 6$. See Fig. 6 for additional details.

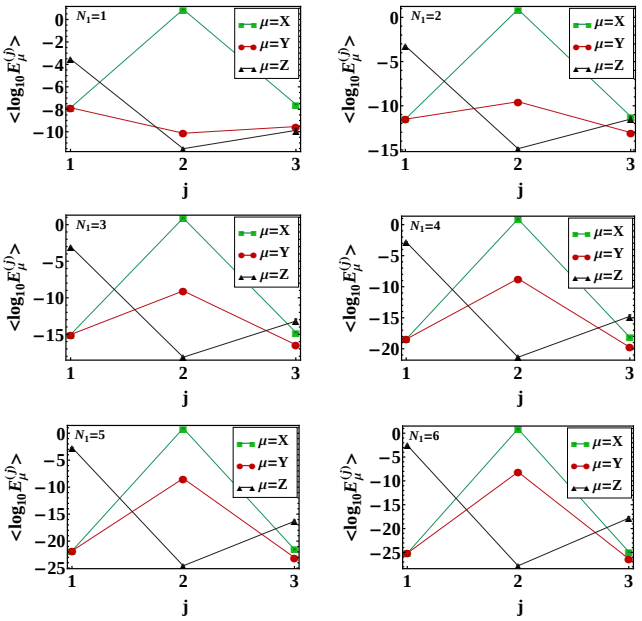

FIG. 19: (color online) Intermediate single-axis errors for $N_2 = 1$. See Fig. 3 for additional details

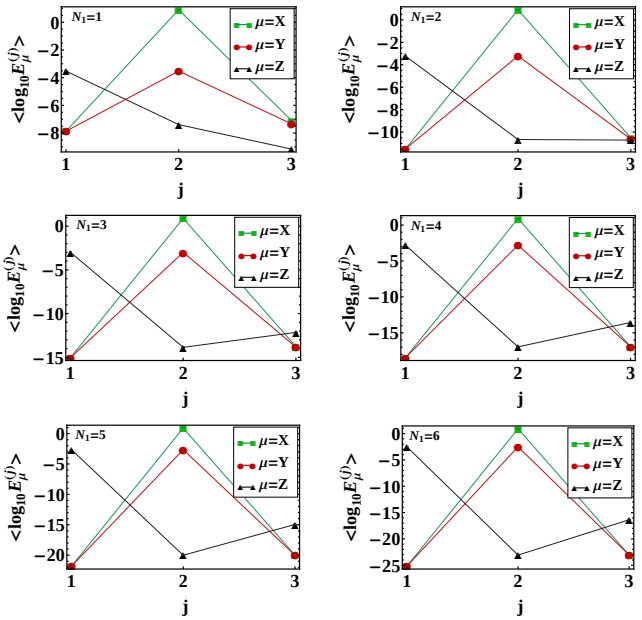

FIG. 20: (color online) Intermediate single-axis errors for $N_2 = 2$. See Fig. 4 for additional details

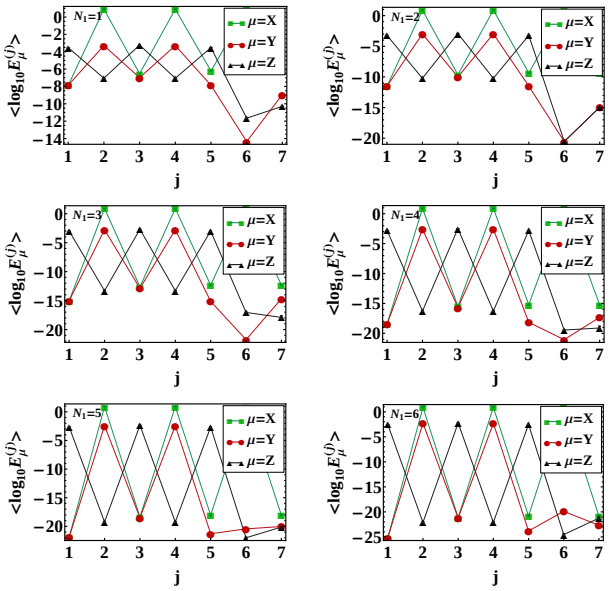

FIG. 21: (color online) Intermediate single-axis errors for $N_2 = 5$. See Fig. 3 for additional details

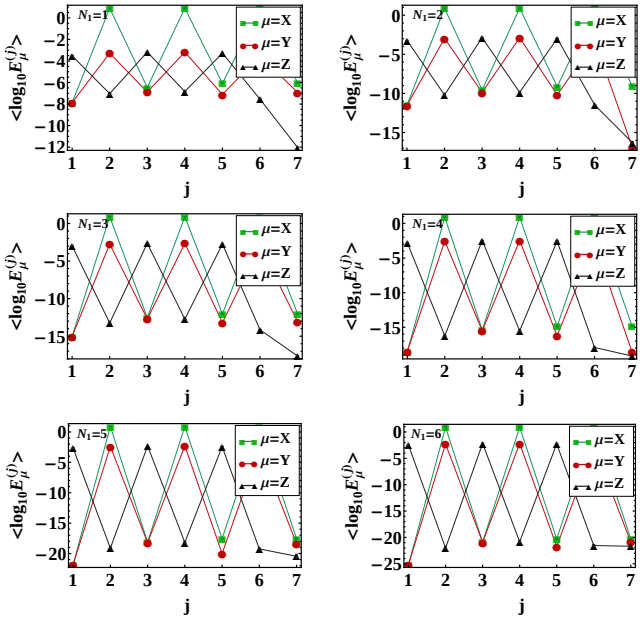

FIG. 22: (color online) Intermediate single-axis errors for $N_2 = 6$. See Fig. 4 for additional details